

Convectively coupled gravity and moisture modes in a simple atmospheric model

By DAVID J. RAYMOND* and ŽELJKA FUCHS, *Physics Department and Geophysical Research Center,
New Mexico Institute of Mining and Technology, Socorro, NM 87801, USA*

(Manuscript received 8 January 2007; in final form 18 June 2007)

ABSTRACT

Recent observational work shows that three factors control the formation of deep convection over tropical oceans; the saturation fraction of the troposphere, surface moist entropy fluxes, and the strength of convective inhibition. A linearized, two-dimensional, non-rotating model of the tropical atmosphere is presented here which incorporates all of these factors into its convective closure in a simplified fashion. Two types of large-scale unstable modes develop in this model, a slowly propagating ‘moisture mode’ which is driven primarily by saturation fraction anomalies, and a convectively coupled ‘gravity mode’ which is governed by anomalies in convective inhibition caused by buoyancy variations just above the top of the planetary boundary layer. The gravity mode maps onto the equatorial Kelvin wave in the earth’s atmosphere and the predicted propagation speed for this mode is close to the observed phase speed of convectively coupled equatorial Kelvin waves. For reasonable parameter values the growth rate peaks at zonal wavenumbers at which Kelvin waves exhibit the greatest spectral energy. The computed vertical structure matches that of observed Kelvin waves, but is produced by a simple sinusoidal vertical heating profile with half-wavelength equal to the depth of the troposphere.

1. Introduction

Recent work indicates that precipitation over warm tropical oceans is controlled by three factors:

(i) Raymond et al. (2003) showed from in situ observations in the tropical east Pacific that the existence of even a weak stable layer just above the planetary boundary layer (PBL) is sufficient to inhibit the development of deep convection and associated precipitation. This confirms earlier results of Firestone and Albrecht (1986) obtained from dropsonde measurements in the tropical Pacific. (See this paper for a summary of earlier results.) Various dynamical processes can generate or remove these stable layers.

(ii) Bretherton et al. (2004) found using passive microwave observations from satellite that precipitation is highly correlated with the saturation fraction (precipitable water divided by saturated precipitable water) of the troposphere. Sobel et al. (2004) came to similar conclusions using data taken near Kwajeleln Island. Results from numerical cloud models also support this conclusion (Lucas et al., 2000; Derbyshire et al., 2004; Raymond and Zeng, 2005).

(iii) In addition to convective inhibition, Raymond et al. (2003) found that infrared brightness temperature (and hence precipitation) is highly correlated with surface moist entropy fluxes in the tropical east Pacific. This is in agreement with similar observations from the equatorial western Pacific by Raymond (1995) and over the entire tropical Pacific by Back and Bretherton (2005).

According to these results, a minimal model of the control of precipitation over warm tropical oceans should therefore include, explicitly or implicitly, the effects of convective inhibition (CIN) due to stability in the 700–850 hPa layer, saturation fraction through the troposphere and surface moist entropy fluxes.

The above list is notable for the absence of convective available potential energy (CAPE) as a control on precipitation. Though negative CAPE certainly precludes deep convective rainfall, the uniformity of the tropical temperature profile means that in many cases this can only occur when the PBL moist entropy is too low. Under such conditions the CIN is also large, which means that negative CAPE is not independent of CIN over warm tropical oceans, and the reduction of CIN results in sufficient CAPE for deep convection under most circumstances. Furthermore, when changes in CAPE are due to temperature changes in the free troposphere, the effect of CAPE control of convection is to damp large-scale disturbances, since convective heating aloft then occurs in regions of larger CAPE and cooler air, resulting

*Corresponding author.
e-mail: raymond@kestrel.nmt.edu
DOI: 10.1111/j.1600-0870.2007.00268.x

in the destruction of available potential energy. Observations in the tropics generally find the opposite, that is, heavy rainfall is correlated with warmer than normal temperatures in the middle and upper troposphere and decreased CAPE (Ramage, 1971; McBride and Frank, 1999).

Linearized models are frequently used to test ideas about the coupling of convection and large-scale dynamics in a minimal and thus easily understood context (e.g. Hayashi, 1970, 1971a,b,c; Lindzen, 1974; Chang, 1977; Emanuel, 1987; Chang and Lim, 1988; Wang and Rui, 1990; Yano and Emanuel, 1991; Emanuel, 1993; Neelin and Yu, 1994; Mapes, 2000; Majda and Shefter, 2001a,b; Fuchs and Raymond, 2002, 2005; Majda et al., 2004; Bony and Emanuel, 2005; Khouider and Majda, 2006, etc.). In the context of an equatorial beta plane model, solutions representing the Madden–Julian oscillation (MJO; Madden and Julian, 1994) and convectively coupled Matsuno modes are generally sought (Matsuno, 1966; Lindzen, 1967; Wheeler and Kiladis, 1999). Prominent among the latter modes is the equatorial Kelvin wave, which is distinguished from the MJO by its smaller zonal scale and faster propagation speed. In the even simpler context of a two-dimensional, non-rotating domain, only convectively coupled gravity waves, which have longitudinal dynamics identical to Kelvin waves and slow-moving moisture modes (Sobel and Horinouchi, 2000; Sobel et al., 2001) are to be expected. The moisture mode works by enhancing precipitation in regions of high humidity, and is thought to operate in easterly waves, monsoon troughs, and other slowly moving tropical disturbances. The moisture mode may even represent some aspects of the MJO (Grabowski and Moncrieff, 2004).

A particularly interesting linearized two-dimensional model is that of Mapes (2000). Following from earlier work on the vertical structure of convective heating in the tropical troposphere (Mapes, 1993; Mapes and Houze, 1995), Mapes (2000) developed a model in which this heating is a superposition of ‘deep convective’ and ‘stratiform’ profiles with fundamental and first harmonic baroclinic mode structures respectively. The convective heating is forced by the relaxation of CIN and the stratiform heating lags the convective heating by a specified interval. The result is an unstable, convectively coupled gravity mode which moves at the observed speed of convectively coupled equatorial Kelvin waves and has their observed vertical structure in temperature. Others (e.g. Majda and Shefter, 2001b; Majda et al., 2004; Khouider and Majda, 2006) have developed variations on the original model of Mapes (2000). Recent observations (Straub and Kiladis, 2002) and cloud resolving simulations of convectively coupled gravity and equatorial Kelvin modes confirm the two-mode vertical structure (Peters and Bretherton, 2006; Tulich et al., 2007). However, questions remain as to the origin of this structure; is it a consequence of the cloud physics of deep convection, which is prone to producing heating in the upper troposphere and cooling below in its decaying phase, or is it more a consequence of large scale dynamics?

We attempt to answer this question by exploring a simplified model of the tropical atmosphere which is vertically resolved and therefore does not presuppose the existence of a two-mode vertical structure. Fuchs and Raymond (2007) developed such a model as an extension to the shallow water models of (Fuchs and Raymond, 2002, 2005). However, the convective closure of these models assumes that precipitation is related solely to the saturation fraction of the troposphere. The purpose of this paper is to modify the forcing of precipitation in the model of Fuchs and Raymond (2007) to include control of precipitation by CIN. In so doing, we incorporate what we believe to be the most important aspect of the equatorial wave model of Mapes (2000). Unlike Mapes (2000), we assume only a simple, first baroclinic mode heating profile in order to avoid imposing a priori a two-mode solution on the dynamics.

Section 2 reexamines observations analysed by Straub and Kiladis (2002) of a Kelvin wave in the tropical east Pacific. Changes made to the model of Fuchs & Raymond (2007) to incorporate CIN control of precipitation appear in Section 3 while parameter values needed by the model are estimated from observation in Section 4. Model results are compared with observations in Section 5 and conclusions are drawn in Section 6.

2. Observed structure of Kelvin waves

The Tropical East Pacific Process Study (TEPPS; Yuter and Houze, 2000) stationed the research vessel *Ronald H. Brown* near 125° W, 8° N for approximately 2 weeks in August 1997 in order to study the convection in the east Pacific intertropical convergence zone (ITCZ). The ship was equipped with a C-band scanning Doppler radar, made in situ weather observations, and launched six radiosondes per day. As reported by Straub and Kiladis (2002), this project observed a particularly clean example of the passage of an equatorial Kelvin wave.

We analysed the radiosonde observations from this project to obtain the time series of CIN and saturation fraction. The few bad soundings in the time series were eliminated and interpolation was made across the resulting data gaps. The deep convective inhibition index (DCIN) was calculated as in Raymond et al. (2003),

$$\text{DCIN} = s_t - s_{\text{bl}} \quad (1)$$

except that the boundary layer entropy s_{bl} was defined as the average moist entropy in the interval (800, 1000) hPa and the threshold moist entropy s_t was taken as the average saturated moist entropy over the interval (750, 800) hPa. These intervals correspond roughly to the trade wind convection layer and the trade wind inversion. The saturation fraction was calculated as the ratio of precipitable water in the sounding to the precipitable water which would have existed for the same temperature profile but 100% relative humidity through the troposphere. In addition, the surface flux of moist entropy F_{es} was estimated using the

simple bulk formula

$$F_{es} = \rho_s C U_e (s_{ss} - s_{bl}), \quad (2)$$

where ρ_s is the surface air density, $C = 0.001$ is the transfer coefficient, $U_e = (U^2 + W^2)^{1/2}$ is the effective surface wind, where U is the actual observed boundary layer wind and $W = 3 \text{ m s}^{-1}$ is a gustiness correction (Miller et al., 1992), and s_{ss} is the saturated moist entropy at the temperature and pressure of the sea surface. A sea surface temperature of 29°C was assumed, which is close to the observed value.

Figure 1 shows a time series of variables derived from TEPPS soundings. The Kelvin wave axis passed the ship at approximately 2000 UTC on 18 August 1997 and was accompanied by half a day of rain. The wind previous to the passage was easterly and it increased in strength and veered to southeasterly as the wave axis approached. At 2000 UTC the wind shifted abruptly to out of the south and then became light westerly. Another short period of rainfall occurred approximately 24 h after the first on-

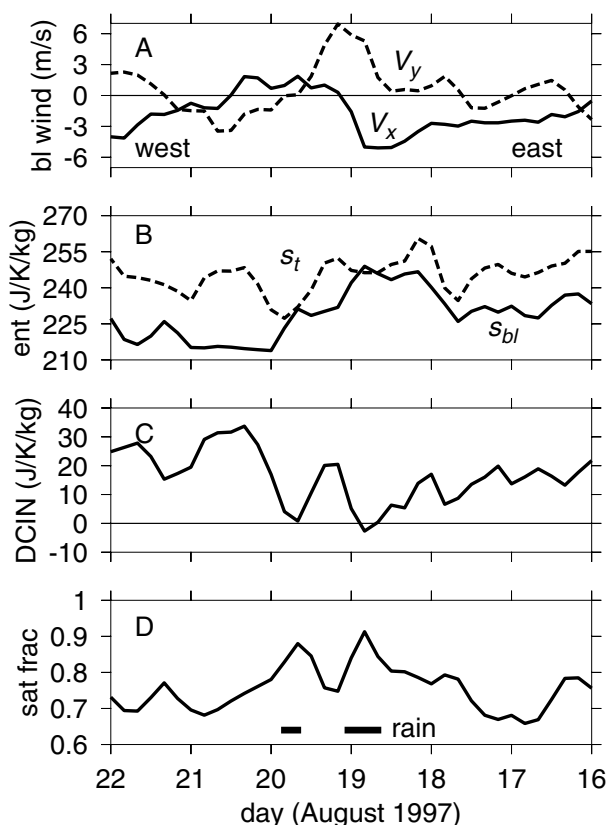


Fig. 1. Time series derived from TEPPS soundings of the passage of a convectively coupled equatorial Kelvin wave through 125°W , 8°N . (a) Zonal (V_x ; westerly positive) and meridional (V_y ; southerly positive) components of the boundary layer wind. (b) Components s_t and s_{bl} of (c) deep convective inhibition DCIN. (d) Saturation fraction of troposphere. The timing of significant rain was derived from Straub and Kiladis (2002). Note the reversed time scale, which makes east to the right in a time to space conversion following the wave.

set of rain. Note that both periods of rainfall were associated with peaks in the saturation fraction near a value of 0.9.

Figure 1 also shows that negative excursions of DCIN coincided with or led the development of rain. From 16 to 18 August the decrease in DCIN was caused primarily by a decrease in the threshold moist entropy s_t . After this time until the passage of the wave axis both s_t and the boundary layer moist entropy s_{bl} increased somewhat, keeping DCIN near zero. Just after the passage of the wave axis s_{bl} decreased significantly, no doubt as the result of convective downdrafts. This resulted in a significant increase in DCIN.

Figure 2 indicates that the increased winds before and during the passage of the wave axis caused a large increase in the surface moist entropy flux. After the wave passage the fluxes dropped to lower values consistent with the weak boundary layer winds at this time. Figure 2 also shows that increased entropy values developed through the lowest 300 hPa as the wave axis approached. Higher values then appeared aloft with a lag of ≈ 1 d. Evidently shallow convection with tops below 700 hPa redistributed surface fluxes efficiently before the passage of the wave axis. As the wave passed, this convection apparently deepened, which allowed the increased values of moist entropy to reach at least 300 hPa. The increase in moist entropy reflects an increase in the

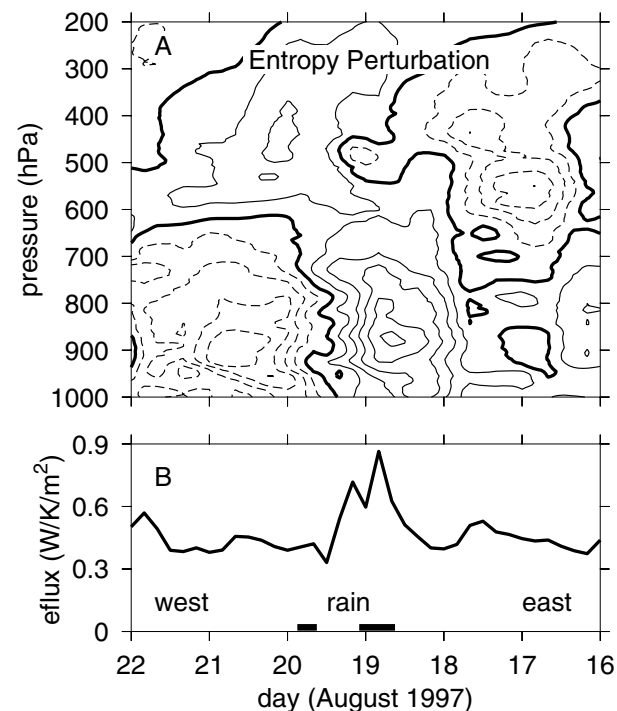


Fig. 2. Time series of (a) the profile of moist entropy perturbation computed relative to the six day period shown (contour interval $4 \text{ J K}^{-1} \text{ kg}^{-1}$, thick line indicates zero perturbation, positive contours solid, negative contours dashed) and (b) the estimated surface moist entropy flux in the Kelvin wave passage. Note the reversed time scale as in Fig. 1.

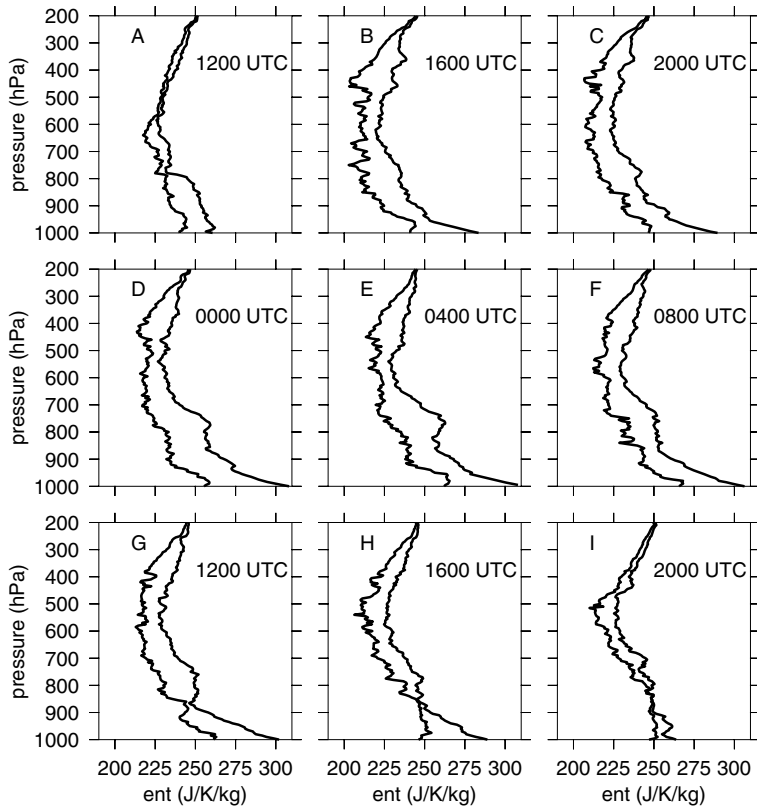


Fig. 3. Ship *Ron Brown* soundings at 4 h intervals on 17 and 18 August 1997 at 125°W, 8°N. The left-hand curve in each plot is the moist entropy and the right-hand curve is the saturated moist entropy.

tropospheric humidity, which in turn is related to the observed increase in saturation fraction during the rain periods.

Figure 3 shows radiosonde sounding plots from the *Brown* at 4 h intervals from 1200 UTC on 17 August 1997 through 2000 UTC on 18 August. The soundings show the development of a stable layer in the saturated moist entropy between 750 and 900 hPa, producing significant DCIN. This stable layer then breaks down, leaving no DCIN at 2000 UTC on 18 August. The decrease in the area between the moist entropy and the saturated moist entropy curves in Fig. 3 reflects the increase in saturation fraction over the period shown in Fig. 1. Note that a deep, well-mixed PBL had developed by 2000 UTC. At no time during this interval is there a lack of CAPE, as defined by a parcel lifted adiabatically from 1000 hPa. However, the depth of the unstable layer, as indicated by the maximum initial height of a parcel exhibiting positive CAPE, increases dramatically over the interval.

The increase in boundary layer moist entropy seen in Fig. 1 is likely due at least partially to the enhanced surface winds, resulting in increased surface moist entropy fluxes. However, a careful examination of Figs. 1 and 2 shows that the increase in boundary layer moist entropy preceded the increase in wind speed, indicating a different initial origin for the enhanced moist entropy. Figure 3 shows that this initial increase occurred in a shallow layer near the surface, probably as a result of boundary layer redevelopment following a previous convective event. The

increase in moist entropy at the lowest levels may therefore be at least partly coincidental and not coupled to the Kelvin wave dynamics.

To summarize the observations, precipitation was linked to both enhanced values of the saturation fraction and small or negative values of DCIN, caused initially by a decrease in the saturated moist entropy just above the planetary boundary layer. The increase in saturation fraction began before the onset of precipitation. This probably resulted at least partially from the enhanced surface fluxes during this time, though some moistening seemed to occur before the surface fluxes increased. Upstream of the wave axis DCIN decreased as a result of the disappearance of the stable layer centred near 750 hPa. Previous to its dissipation, the entropy excess was confined to below 700 hPa. Only after the stable layer's demise did the entropy increase above this level. The deep convection and resulting precipitation were thus related to the moistening of the atmosphere, but they were delayed approximately one day by the existence of the stable layer. Therefore, DCIN appears to have played a significant role in the timing of the precipitation in this event.

The above results are derived from a single Kelvin wave. Roundy and Frank (2004) developed a climatology of equatorial waves from outgoing longwave radiation (OLR) and satellite-derived precipitable water data. A particularly interesting result of this work is that while the Kelvin wave signal is as strong as those of equatorial Rossby waves and the MJO in a

wavenumber–frequency power spectral plot of OLR, the Kelvin wave is much weaker than the other modes in an analogous precipitable water plot. (see their Figs. 2 and 3). Thus, for a given anomaly in upper level cloudiness, the anomaly in precipitable water is much less in Kelvin waves than in the other mentioned modes. This is in contrast to the above-described TEPPS case and suggests that the TEPPS observations may not be completely representative.

3. Model

The model of Fuchs and Raymond (2007) found both slowly propagating modes associated with moisture anomalies and more rapidly moving convectively coupled gravity modes. However, only the moisture modes were unstable. The equatorial wave model of Mapes (2000) illustrates the importance of CIN in the destabilization of gravity modes. Perhaps two fundamentally different destabilization mechanisms exist for tropical wave modes; tropospheric humidification as explored by Sobel et al. (2001) and Fuchs and Raymond (2002, 2005, 2007), and the relaxation of CIN investigated by Mapes (2000). We seek to incorporate both of these mechanisms into a minimal model which displays their workings in as simple and clear a fashion as possible. We accomplish this with an extension of the model of Fuchs and Raymond (2007, hereafter FR).

The two-dimensional, linearized, Boussinesq system of FR leads to an equation for the vertical velocity w

$$\frac{d^2 w(z)}{dz^2} + m^2 w(z) = \frac{k^2}{\omega^2} S_B(z) \quad (3)$$

and polarization relations for the buoyancy b and the scaled moist entropy perturbation e

$$b = (i/\omega)(S_B - \Gamma_B w) \quad (4)$$

$$e = (i/\omega)(S_E - \Gamma_E w), \quad (5)$$

where the x and t dependence takes the form $\exp[i(kx - \omega t)]$ with k and ω being the zonal wavenumber and frequency. The vertical wavenumber is $m = k\Gamma_B^{1/2}/\omega$ and Γ_B is the (constant) square of the Brunt-Väisälä frequency. The scaled potential temperature perturbation or buoyancy is defined $b = g\theta'/T_R$, where θ' is the perturbation potential temperature and $T_R = 300$ K is a constant reference temperature. The moist entropy perturbation is scaled by g/C_p where g is the acceleration of gravity and C_p is the specific heat of air at constant pressure. The quantity $\Gamma_E = de_0/dz$ where $e_0(z)$ is the scaled ambient profile of moist entropy. The scaled moist entropy source term is denoted S_E .

As in FR, we assume that

$$S_B = (m_0 B/2) \sin(m_0 z) \quad z < h, \quad (6)$$

where B is independent of z and $m_0 = \pi/h$, h being the height of the tropopause. We therefore do not allow the shape of the heating profile to vary with the phase of the wave, thus neglecting the

differences in heating profiles between convective and stratiform regions postulated by Mapes (2000) and others.

The difference between the model of FR and the present model lies entirely in the form of B . The vertically integrated heating anomaly due to the scaled precipitation P and radiative cooling rate R anomalies is assumed to take the form

$$\int_0^h S_B dz = B = P - R = \alpha(1 + \varepsilon) \times \int_0^h q(z) dz + \mu_{\text{CIN}}(e_s - e_t), \quad (7)$$

where α is a moisture adjustment rate. The variable ε quantifies the effect of cloud-radiation interactions which are assumed to cause a radiative heating anomaly in phase with precipitation (see Fuchs and Raymond, 2002). The profile of scaled mixing ratio anomaly is given by

$$q(z) = e(z) - b(z) \quad (8)$$

and has the scaling factor $gL/(C_p T_R)$ where L is the latent heat of condensation.

The first term on the right-hand side of eq. (7) is proportional to the precipitable water anomaly and constitutes the entire heating in the model of FR. We use precipitable water rather than the saturation fraction as suggested by Bretherton et al. (2004), which is equivalent if the saturated precipitable water does not change significantly. We have verified that variations in saturated precipitable water have only minor effects in our model, and we therefore have ignored these because of the complications that they introduce.

The second term is new, and represents the effect of CIN on heating. The quantity e_s is the scaled perturbation in boundary layer moist entropy $e_s = s'_{\text{bl}}g/C_p$, while e_t is a similarly scaled threshold value of the perturbation moist entropy. Thus, the contribution to precipitation and heating is positive when $e_s > e_t$ and negative otherwise. The constant μ_{CIN} governs the sensitivity of precipitation rate to deep convective inhibition.

We set e_t equal to the saturated moist entropy perturbation at elevation Dh , where D is this elevation expressed as a fraction of the tropopause height h . In the simplified thermodynamic scheme of FR, e_t is related to the buoyancy anomaly $b(D)$ at elevation Dh by

$$e_t = \left[1 + \frac{L}{C_p} \left(\frac{\partial r_s}{\partial T} \right)_p \right] b(D) \equiv \lambda_t b(D), \quad (9)$$

where r_s is the saturation mixing ratio at elevation Dh . In tropical conditions near 800 hPa the dimensionless parameter $\lambda_t \approx 3.5$, a result easily verified from a skew T -log p chart.

The boundary layer moist entropy is subject to a balance primarily between a positive tendency due to surface moist entropy fluxes and a negative tendency due to convective downdrafts and turbulent entrainment of dry air into the boundary layer. The details of this balance are difficult to represent in a simple model, due to the complexity of the processes involved. Here we make

the simple, but incomplete assumption that stronger surface wind speeds cause increased surface evaporation which results in enhanced boundary layer moist entropy,

$$e_s = \lambda_s E. \tag{10}$$

The quantity λ_s is a constant and E is the surface evaporation rate anomaly scaled with the same scale factor as q . The evaporation rate anomaly takes the form

$$E = \frac{C \Delta q U u_s}{(U^2 + W^2)^{1/2}}, \tag{11}$$

where C is the surface bulk transfer coefficient, Δq is the scaled difference between the saturation mixing ratio at the sea surface temperature and pressure and the subcloud mixing ratio, U is the ambient zonal wind at the surface, $W \approx 3 \text{ m s}^{-1}$ is a constant needed to account for gustiness (Miller et al., 1992), and u_s is the perturbation surface zonal wind obtained from w via mass continuity. Fortunately, as we show below, fluctuations in the surface moist entropy have little effect on the fundamental dynamics of our convectively coupled gravity modes.

To summarize, the vertically integrated heating can be written as the sum of three contributions, $B = P_1 + P_2 - R$, where

$$P_1 = \alpha \int_0^h q(z) dz \tag{12}$$

$$P_2 = \mu_{\text{CIN}} [\lambda_s E - \lambda_t b(D)] \tag{13}$$

$$R = -\alpha \varepsilon \int_0^h q(z) dz. \tag{14}$$

We further subdivide P_2 into a part P_{2s} having to do with surface flux variations

$$P_{2s} = \mu_{\text{CIN}} \lambda_s E \tag{15}$$

and a part P_{2t} related to variations in the buoyancy above the boundary layer

$$P_{2t} = \mu_{\text{CIN}} \lambda_t b(D). \tag{16}$$

We finally note that the vertical integral of the moist entropy source term S_E can be related to the scaled surface evaporation rate E and radiative cooling rate R anomalies

$$\int_0^h S_E dz = E - R \tag{17}$$

in the absence of significant surface sensible heat fluxes.

Solution of (3) with an upper radiation boundary condition yields

$$w(z) = \frac{m_0 B}{2\Gamma_B(1 - \Phi^2)} \left[\sin(m_0 z) + \Phi \exp\left(-\frac{i\pi}{\Phi}\right) \sin(mz) \right] \tag{18}$$

and substitution of this into (4) results in

$$b(z) = -\frac{i m_0 B}{2\alpha \kappa(1 - \Phi^2)} \left[\Phi \sin(m_0 z) + \exp\left(-\frac{i\pi}{\Phi}\right) \sin(mz) \right] \tag{19}$$

for the troposphere, where $\kappa = h\Gamma_B^{1/2} k/(\pi\alpha)$ is the dimensionless wavenumber and where $\Phi = \omega/(\alpha\kappa) = m_0/m$ is the dimensionless phase speed. Combining (4), (5), (7) and (8) results in an equation for the vertically integrated heating B ,

$$B = -\frac{i\kappa\Phi + \varepsilon}{1 - i\kappa\Phi} \mu_{\text{CIN}} [\lambda_s E - \lambda_t b(D)] + \frac{1 + \varepsilon}{1 - i\kappa\Phi} \left[E + (1 - \Gamma_M) \int_0^h \Gamma_B w dz \right], \tag{20}$$

where Γ_M is a version of the gross moist stability of Neelin and Held (1987) and is defined here as

$$\Gamma_M = \int_0^h \Gamma_E w dz / \int_0^h \Gamma_B w dz. \tag{21}$$

Finally, combining (18)–(20) with the help of (9)–(11) results in the dispersion relation

$$\kappa\Phi^3 + i\Phi^2 - \kappa\Phi - i + i(1 + \varepsilon)(1 - \Gamma_M)F(\Phi) - \Lambda G(\Phi)/\kappa + (\varepsilon + i\kappa\Phi)[\chi_t L(D, \Phi) + \chi_s \Lambda G(\phi)/(1 + \varepsilon)]/\kappa = 0, \tag{22}$$

where the dimensionless WISHE parameter Λ (wind-induced surface heat exchange; Yano and Emanuel, 1991) is defined

$$\Lambda = \frac{(1 + \varepsilon)m_0 C \Delta q U}{2\alpha \Gamma_B^{1/2} (U^2 + W^2)^{1/2}}. \tag{23}$$

The dimensionless parameters $\chi_t = \lambda_t \mu_{\text{CIN}} m_0 / (2\alpha)$ and $\chi_s = \lambda_s \mu_{\text{CIN}}$ represent the sensitivity of precipitation to buoyancy anomalies above the PBL and to surface entropy flux variations. Setting $\chi_s = \chi_t = 0$ returns us to the dispersion relation of FR.

FR assumed that the scaled ambient moist entropy $e_0(z)$ takes a piecewise linear form in the troposphere, which results in a gross moist stability Γ_M equal to

$$\Gamma_M = \frac{\Delta e [2H - 1 + \cos(\pi H) + K(H, \Phi)]}{2H(1 - H)F(\Phi)} \approx \frac{\Delta e [2H - 1 + \cos(\pi H)]}{2H(1 - H)}. \tag{24}$$

As described by FR, the parameter H is the fractional height relative to the tropopause of the minimum in the ambient moist entropy profile and Δe is the scaled difference between the surface and tropopause values of moist entropy (assumed to be the same) and the minimum value at this height. The approximated form on the right-hand side of eq. (24) is valid when $|\Phi|^2 \ll 1$, as is true for all of the interesting modes studied here. Note that this approximate form is real and independent of Φ , which means that Γ_M can be treated as a constant external parameter under these conditions.

The auxiliary functions $F(\Phi)$, $G(\Phi)$, $K(H, \Phi)$ and $L(D, \Phi)$ are defined

$$F(\Phi) = 1 + \frac{\Phi^2}{2} \exp\left(-i\frac{\pi}{\Phi}\right) \left[1 - \cos\left(\frac{\pi}{\Phi}\right) \right], \tag{25}$$

$$G(\Phi) = 1 + \exp(-i\pi/\Phi), \tag{26}$$

$$K(H, \Phi) = \Phi^2 \exp\left(-i \frac{\pi}{\Phi}\right) \times \left[H - 1 - H \cos\left(\frac{\pi}{\Phi}\right) + \cos\left(\frac{\pi H}{\Phi}\right) \right], \quad (27)$$

$$L(D, \Phi) = \exp(-i\pi/\Phi) \sin(\pi D/\Phi) + \Phi \sin(\pi D). \quad (28)$$

4. Parameter estimation

Table 1 lists the dimensionless free parameters occurring in the dispersion relation (22), and the range of values used in the present work. The first three of these, ε , H and Δe , are assigned the values used in FR, resulting in $\Gamma_M \approx 0$. Here we consider the WISHE parameter Λ and the three additional parameters associated with the control of convection by CIN; the scaled height of the controlling stable layer for convection D , the sensitivity of precipitation to stable layers at this elevation χ_t and the sensitivity of precipitation to surface moist entropy fluxes χ_s .

Certain dimensional variables are needed to compute these non-dimensional parameters. These, with their assumed values, include the depth of the troposphere $h = 15$ km, the Brunt-Väisälä frequency $\Gamma_B^{1/2} = 0.01 \text{ s}^{-1}$ and the moisture adjustment rate $\alpha = (1 \text{ d})^{-1}$. The fundamental baroclinic mode vertical wavenumber is $m_0 = \pi/h = 2.09 \times 10^{-4} \text{ m}^{-1}$ and the speed of hydrostatic gravity waves with this vertical structure is $\Gamma_B^{1/2}/m_0 = 48 \text{ m s}^{-1}$.

Examination of Fig. 1 suggests that the zonal wind averaged before and after the passage of the Kelvin wave is about 2 m s^{-1} from the east. Using the other parameter values assumed in FR, this leads to a dimensionless WISHE parameter of $\Lambda \approx -0.28$. We also are interested in the simpler case in which there are no mean easterlies. According to (23), $\Lambda = 0$ in this case. Observations show that stable layers occur frequently near an elevation of 2 km in the tropics (Firestone and Albrecht, 1986; Raymond et al., 2003). For $h = 15$ km, this corresponds to $D = 0.17$.

Table 1. Non-dimensional free parameters in the dispersion relation (22). WISHE indicates wind-induced heat exchange while CIN means convective inhibition. The typical values used in the present calculations are given in the second column

Parameter	Value	Comment
ε	0.2	Cloud-radiation interaction
H	0.5	Scaled height of moist entropy minimum
Δe	0.26	Scaled magnitude of entropy minimum
Γ_M	≈ 0	Approximate gross moist stability
Λ	0, -0.28	WISHE parameter
D	0.17	Scaled height of CIN threshold layer
χ_s	7	Sensitivity to surface entropy flux
χ_t	12	Sensitivity to stable layers

The next easiest parameter to estimate is χ_s . According to (12) and (13),

$$\chi_s = \lambda_s \mu_{\text{CIN}} = \frac{\partial P}{\partial E}, \quad (29)$$

where the buoyancy at $z = Dh$ and the precipitable water are held constant. Measurements in the east Pacific ITCZ during the EPIC project (Raymond et al., 2004) showed the dependence of infrared brightness temperature T_{IR} on both precipitation rate and surface moist entropy flux F_{es} at constant DCIN. Since the sensible heat flux is much less than the latent heat flux at the ocean surface, the entropy flux can be related approximately to the evaporation rate. Using these measurements we find that

$$\frac{\partial P}{\partial E} \approx \frac{L}{T_R} \frac{\partial T_{IR}/\partial F_{es}}{\partial T_{IR}/\partial P} \approx 1.7 \quad (30)$$

for EPIC. Unfortunately, these measurements were uncontrolled for precipitable water. However, Back and Bretherton (2005) used satellite measurements over the entire Pacific ITCZ to infer the dependence of precipitation on boundary layer wind speed U for different values of column relative humidity or saturation fraction, that is, precipitable water divided by saturated precipitable water. Values of $\partial P/\partial E$ ranged from 2 to 9 as the saturation fraction increased from 0.71 to 0.80. (We used a conversion factor $\partial U/\partial E = 2 (\text{m s}^{-1})/(\text{mm d}^{-1})$ based on plausible bulk flux formula parameters.) Unfortunately, these numbers are not controlled for convective inhibition. Given the uncertainties in both sets of numbers, we tentatively assume a plausible range of values for χ_s to be $2 < \chi_s < 8$.

Less certain is the evaluation of χ_t . Perhaps the easiest route to the determination of this parameter is an indirect one via the definition of χ_s and an independent estimate of λ_s : from the definition of χ_t and (29) we have

$$\chi_t = \frac{\lambda_t \mu_{\text{CIN}} m_0}{2\alpha} = \frac{\lambda_t \chi_s m_0}{2\alpha \lambda_s}. \quad (31)$$

As (10) shows, λ_s can be written

$$\lambda_s = \frac{\partial e_s}{\partial E} \approx \rho_{\text{bl}} \frac{\partial s_{\text{bl}}}{\partial F_{es}}, \quad (32)$$

where the partial derivative is taken at constant precipitable water and $b(D)$ and where ρ_{bl} is the boundary layer air density. From Figs. 1 and 2 we note that the boundary layer entropy and surface fluxes increase as the Kelvin wave approaches the ship, with $\Delta s_{\text{bl}} \approx 15 \text{ J K}^{-1} \text{ kg}^{-1}$ and $\Delta F_{es} \approx 0.4 \text{ J K}^{-1} \text{ m}^{-2} \text{ s}^{-1}$, resulting in $\lambda_s \approx 45 \text{ s m}^{-1}$ if $\rho_{\text{bl}} = 1.2 \text{ kg m}^{-3}$.

One can argue that the above estimate is flawed in that the mean value of boundary layer moist entropy (or equivalent potential temperature) actually does not change much in going from convectively quiescent to active regions; the standard deviation of the moist entropy simply increases, as there are higher values due to the stronger winds and surface fluxes which typically occur under these conditions, and there are lower values due to the deposition of low entropy air in the boundary layer by convective downdrafts (see Raymond, 1995). Averaging the boundary

layer entropy over the full passage of the Kelvin wave (see Fig. 1) supports this view. Thus an alternative estimate on this basis would be $\lambda_s \approx 0$.

For the purposes of this paper we pick intermediate values with the range $15 \text{ s m}^{-1} \leq \lambda_s \leq 30 \text{ s m}^{-1}$. Together with the condition $2 \leq \chi_s \leq 8$, the region in the $\chi_s - \chi_t$ plane to be studied is shown by the unshaded area in Fig. 10. As a control case, we pick $\chi_s = 7$ and $\chi_t = 12$. This choice is represented by the black dot in Fig. 10.

5. Results

We first discuss results for the parameter set presented in table 1 with $\Lambda = 0$. In this case there are no mean easterlies, WISHE is turned off, and the value of λ_s becomes irrelevant. In other words, surface heat flux variations have no modulating effect on convective heating in the linearized case presented here and the DCIN is controlled exclusively by variations in the saturated moist entropy at the top of the PBL.

The roots of the dispersion relation (22) were obtained numerically. Fig. 4 shows the phase speed $\text{Re}(\omega)/k$ and the growth rate

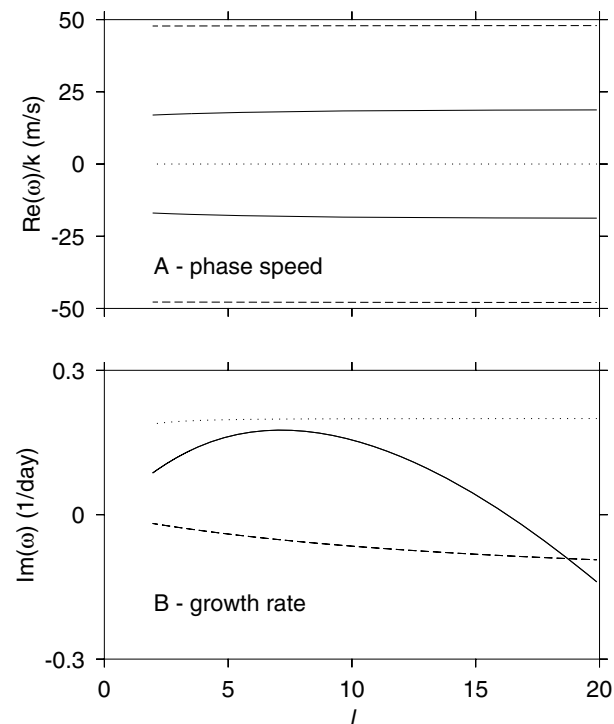


Fig. 4. Real part of phase speed (upper panel) and imaginary part of frequency (lower panel) for the control case with $\Lambda = 0$. The dotted lines show the moisture mode, solid lines show the eastward and westward moving gravity modes, and short-dashed lines show rapidly moving gravity waves with fundamental baroclinic mode structure. Note that the growth rates of eastward and westward modes coincide in this plot.

$\text{Im}(\omega)$ as a function of zonal wavenumber l , defined as the circumference of the earth divided by the zonal wavelength. Three types of modes are seen; a single stationary moisture mode unstable over a wide range of wavenumbers; eastward and westward moving convectively coupled gravity modes with phase speeds near 18 m s^{-1} and maximum growth rates near $l = 7$; and fast but decaying gravity modes moving to the east and west with phase speeds near the fundamental baroclinic mode speed of 48 m s^{-1} . In the absence of mean easterlies the modes exhibit east-west symmetry. Not shown are higher harmonics of convectively coupled gravity modes which move with speeds near 10 m s^{-1} and have much lower growth rates than the other modes.

Due to the beta effect near the equator, the westward-moving modes have no analog in the earth's atmosphere. However, equatorially trapped Kelvin waves have the same zonal dynamics and dispersion relations as the eastward-moving gravity modes as long as surface friction is neglected. Comparison with the observational results of Wheeler and Kiladis (1999) and Roundy and Frank (2004) shows good agreement between the illustrated convectively coupled mode's phase speed and the observed equatorial Kelvin waves. Furthermore, the maximum in the computed growth rate near $l = 7$ agrees well with the wavenumber of maximum Kelvin wave spectral power shown in these papers.

The vertical structure of the eastward-moving convectively coupled gravity mode is in good agreement with the observed zonal-height structure of Kelvin modes. Figure 5 shows the convective heating and buoyancy anomalies in the $x - z$ plane for the eastward-moving gravity mode. The characteristic 'boomerang' structure noted by Wheeler et al. (2000) and Straub and Kiladis (2002) in observations and by Peters and Bretherton (2006) and Tulich et al. (2007) in cloud resolving numerical simulations is seen in our model result, with westward-tilting contours of buoyancy anomaly up to the tropopause, topped by eastward-tilting contours in the stratosphere. The level at which the tilt changes sign is somewhat higher than observed by Straub and Kiladis (2002). This could be related to the simplified heating profile used in our model. Positive buoyancy anomalies are seen in the middle and upper troposphere in the region of maximum convective heating, with negative anomalies below. This is consistent with the net generation of available potential energy by the heating. We note that the gravity mode structure seen here is absent in the decaying gravity modes of FR.

The origin of the buoyancy anomaly structure becomes clear when the solution for the anomaly is split into homogeneous and inhomogeneous parts, represented respectively by the terms proportional to $\sin(mz)$ and $\sin(m_0z)$ in (19). These are shown in Figs. 6 and 7. The inhomogeneous part of the buoyancy anomaly leads the rightward-moving heating maximum and has a simple, vertically oriented structure. The homogeneous part is larger in amplitude and more complex, with a tilt to the west below the tropopause ($z/h < 1$) and an eastward tilt above ($z/h > 1$). The

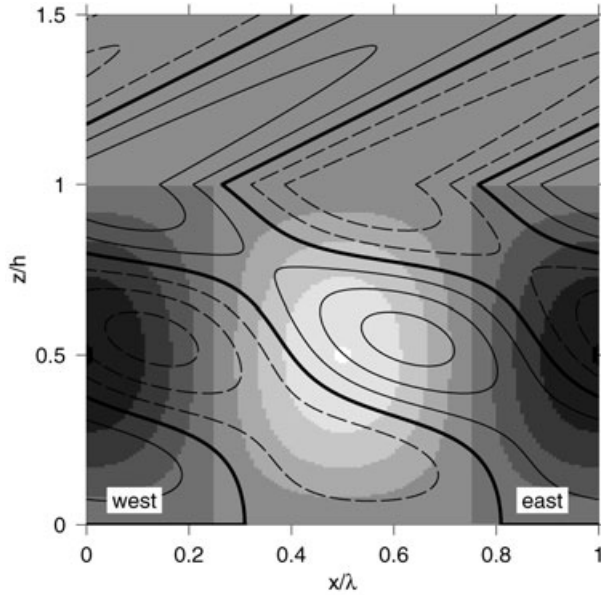


Fig. 5. Heating anomaly (shading with lighter indicating positive values) and perturbation buoyancy (or temperature; solid contours indicating positive values, dashed contours negative, with the heavy contour indicating zero) for the convectively coupled gravity mode with no WISHE ($\Lambda = 0$) at the zonal wavenumber of greatest instability $l = 7$, as a function of wave phase (x/λ where λ is the horizontal wavelength) and scaled height z/h . The contour interval is arbitrary.

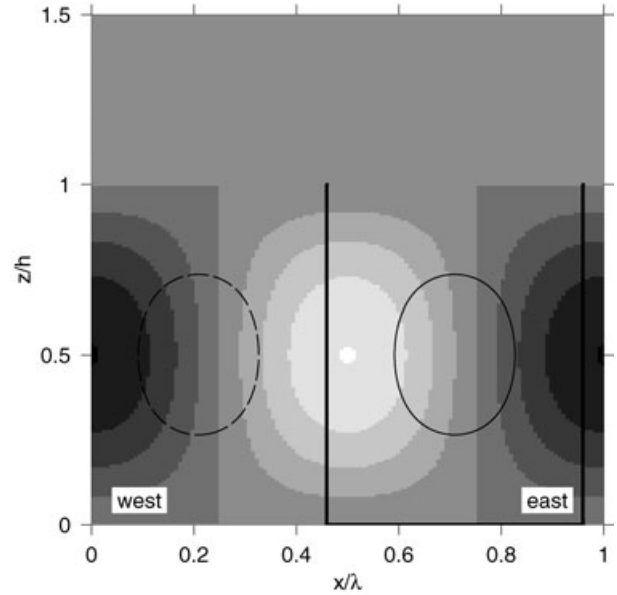


Fig. 7. As in Fig. 5 except just the inhomogeneous part of the buoyancy.

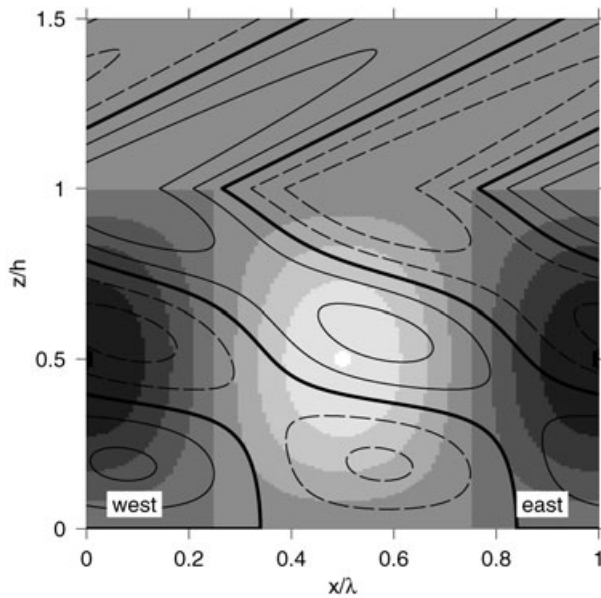


Fig. 6. As in Fig. 5 except just the homogeneous part of the buoyancy.

solution above the tropopause is $b \propto \exp[i(kx - mz)]$, which explains the eastward tilt. The vertical wavenumber m has a negative imaginary part, which causes a decrease in amplitude with height. This part of the solution is consistent with an up-

ward radiation boundary condition of an exponentially growing solution.

Below the tropopause the sinusoidal form of homogeneous part of the buoyancy anomaly can be written in terms of complex exponentials as $b \propto \exp[i(kx + mz)] - \exp[i(kx - mz)]$. Near the surface the exponential terms have nearly the same amplitude and the resulting interference pattern therefore has nearly vertically aligned constant phase lines. However, at higher altitudes (but below the tropopause) the negative imaginary part of m causes the first term to dominate, resulting in the westward tilt of constant phase lines seen in Fig. 6.

The tilts of constant phase lines below the tropopause depend in this model on the fact that the mode is growing in amplitude with time. This explains why the tilted structure was not seen in the decaying modes of FR. One might argue that non-intensifying convectively coupled modes should therefore exhibit non-tilted constant phase lines below the tropopause. This would be true if such steady modes exhibited no dissipation. However, it is easy to demonstrate that a model in which Newtonian damping stabilizes an otherwise growing mode retains the spatial structure of the undamped mode. Therefore, as long as the mode is either intensifying or is neutral due to Newtonian or similar damping, the tilted structure below the tropopause is robust.

Figure 8 shows the pattern of vertical velocity relative to the pattern of heating. The vertical velocity is mostly proportional to the heating as expected, but deviations from this balance show a westward tilt in the troposphere, exhibiting enhanced upward motion at low levels on the east side of the heating and enhanced ascent at high levels on the west side, as is seen in observed Kelvin waves.

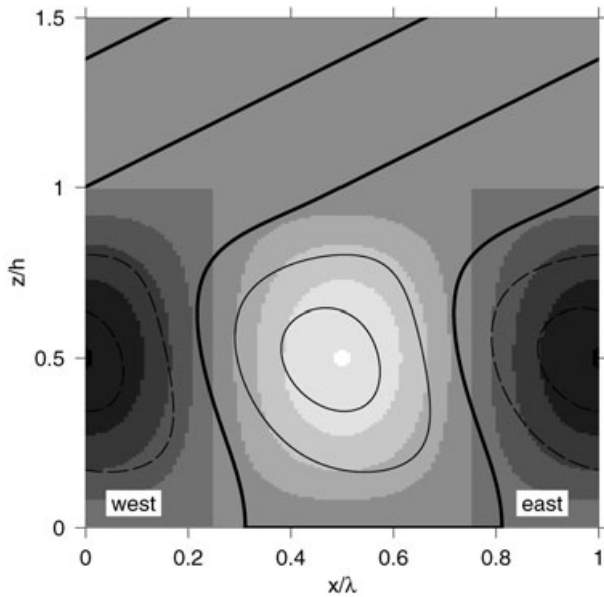


Fig. 8. As in Fig. 5 except that the contours show vertical velocity instead of buoyancy anomaly.

With the above-noted tilts, our model reproduces the observed vertical structure of convectively coupled equatorial Kelvin waves. This is true in spite of the fact that the shape of vertical profile of heating is (by design) independent of wave phase. Our results therefore challenge the assertion of Mapes (2000), Majda and Shefter (2001b), etc., that the boomerang structure of equatorial Kelvin waves is due to phase-lagged bimodal convective heating.

We now explore the effects of turning on WISHE in the model. Figure 9 shows the phase speeds and growth rates of all modes for the parameter choices shown in Table 1 with $\Lambda = -0.28$, corresponding to mean easterly flow. The changes in comparison to the non-WISHE case shown in Fig. 4 are fairly minor; the moisture mode now moves to the east for long wavelengths and the eastward-moving convectively coupled mode has a slightly higher maximum growth rate at a somewhat longer wavelength than the westward-moving mode. The variations in phase speed, maximum growth rate, and wavenumber for this maximum are shown as a function of λ_s and λ_v for the eastward-moving convectively coupled mode in Fig. 10. The changes in the structure of the convectively coupled gravity modes compared to the non-WISHE case are very small and are not shown.

The moisture mode has a very different vertical structure than the convectively coupled gravity mode. Figure 11 illustrates the heating and buoyancy anomalies for the moisture mode with wavenumber $l = 2$ and mean easterly flow. As Fig. 9 shows, the moisture mode at this wavenumber propagates to the east as a result of the WISHE mechanism. This is reflected in the eastward shift of the heating maximum relative to the buoyancy maximum. The buoyancy anomaly does not exhibit the tilted structure seen in the gravity mode in the troposphere. However, in

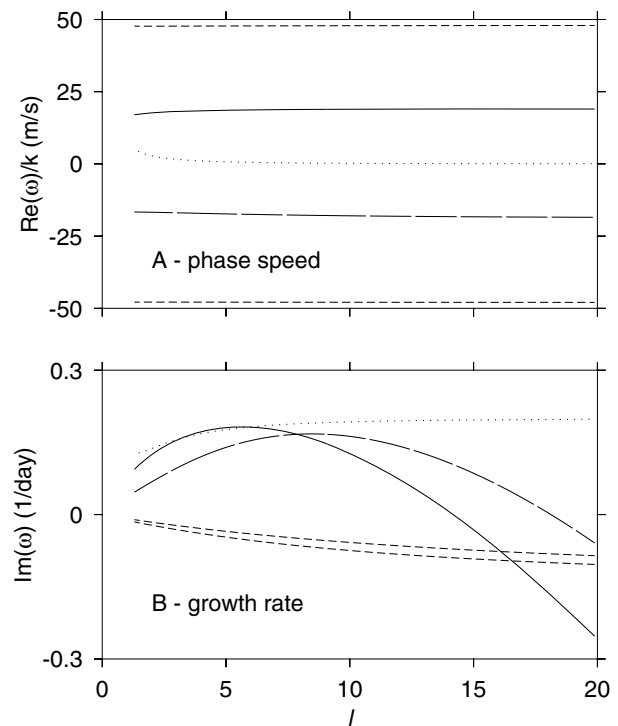


Fig. 9. As in Fig. 4 except that WISHE is turned on ($\Lambda = -0.28$). The solid line represents the eastward-moving convectively coupled gravity mode while the long-dashed line represents the corresponding westward-moving mode.

the stratosphere an eastward tilt is seen, as is to be expected of an eastward-moving disturbance. The vertical velocity accurately mirrors the heating in the troposphere for this mode, and is not shown for this reason. Moisture mode growth rates are relatively insensitive to variations in χ_s and χ_r , though increasing χ_s tends to decrease eastward propagation speeds.

The slow eastward movement at small wavenumbers of the moisture mode tempts us to identify this mode with the MJO. However, the growth rate of this mode decreases somewhat at long wavelengths and there are many other factors to be considered in relation to the MJO, such as the questionable existence of mean equatorial easterlies, the possible role of meridional moisture gradients (Sobel et al., 2001), off-equatorial vortical structure, etc. Nevertheless, the suggestion that the mechanism of moisture mode instability may play some role in the dynamics of the MJO remains plausible, especially given the results of Grabowski (2003) and Grabowski and Moncrieff (2004) using fine-scale numerical modeling, which show that the MJO-like disturbance in their model vanishes when tropospheric moisture variability is suppressed. As Sobel et al. (2001) point out, many slowly propagating convective modes in the tropics exhibiting a broad range of scales may depend on the moisture mode mechanism. This is consistent with the lack of scale selectivity seen in this mode.

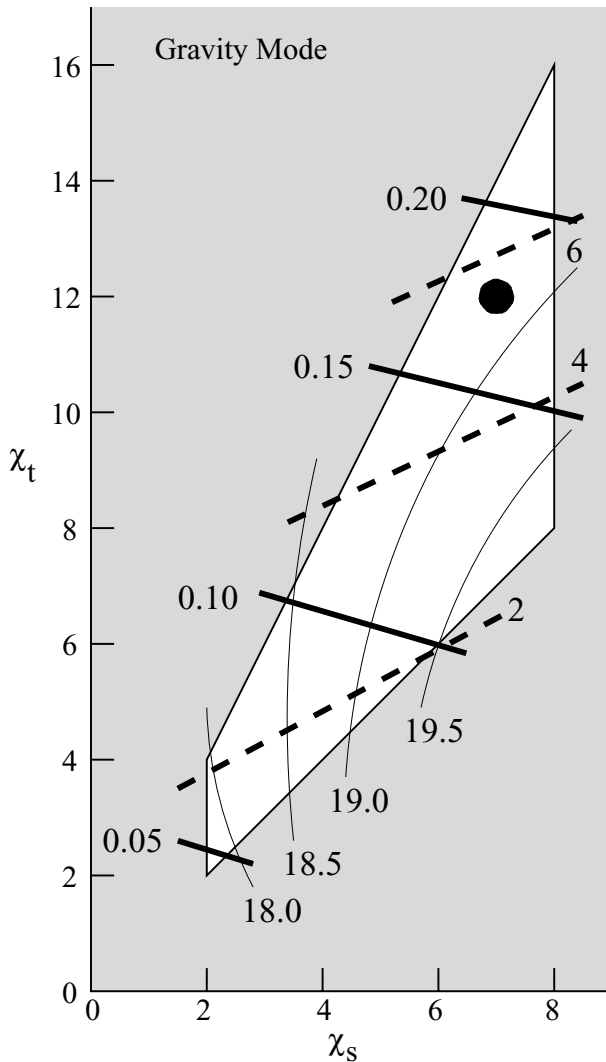


Fig. 10. The allowed range of parameters χ_s and χ_t suggested by observation is encompassed by the polygon. The thick solid contours represent values of maximum growth rate for convectively coupled gravity modes in units of inverse days, the thin solid contours represent phase speed in metres per second, and the thick dashed contours indicate the zonal wavenumber for which the growth rate is maximal. The dot represents the parameter set in Table 1.

The identification of the eastward-moving convectively coupled gravity mode with the equatorial Kelvin wave is more robust. This mode is only modified slightly by WISHE and is relatively insensitive to variations in χ_s . Increasing χ_s tends to increase the ratio of P_{2s} to P_{2t} . The greatest parameter sensitivity of the gravity mode is to variations in χ_t , with increasing values of this parameter associated with higher growth rate maxima occurring at shorter wavelengths, as is illustrated in Fig. 10. Setting $\chi_t = 0$ causes the gravity mode to decay.

Figure 12 shows the various contributions to the total precipitation as a function of wave phase for the eastward-moving

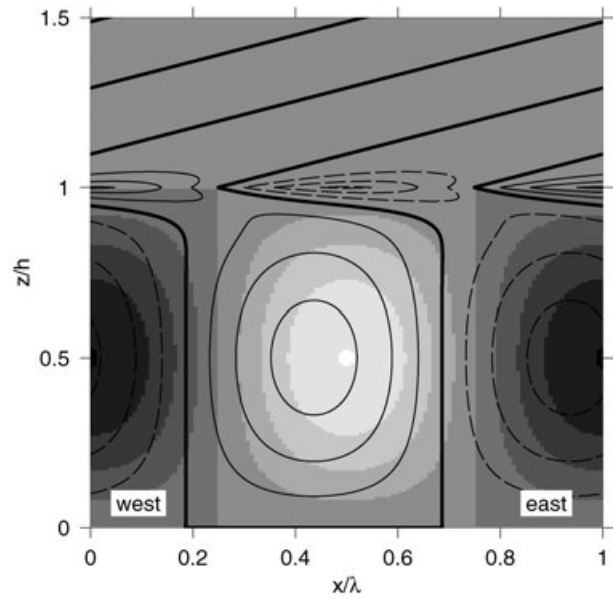


Fig. 11. Heating rate and buoyancy anomaly as in Fig. 5 except for moisture mode with wavenumber $l = 2$ and with WISHE turned on.

convectively coupled gravity mode at zonal wavenumber $l = 5.5$, which is the wavenumber of maximum growth rate for the eastward-moving gravity mode with WISHE. Most of the precipitation associated with this wave comes from P_{2t} , that is, the reduction of CIN as a result of wave-induced cooling above the PBL. There is a significant contribution to the precipitation from P_{2s} , but this has little effect on the wave growth rate as the resulting heating is in quadrature with the dominant heating associated with P_{2t} . This is consistent with the result that turning off WISHE causes only minor changes in wave behaviour. This component of the heating also has only minor effect on the propagation speed of the mode since the vertical wavelength of the homogeneous part of the solution, which determines the propagation speed, is

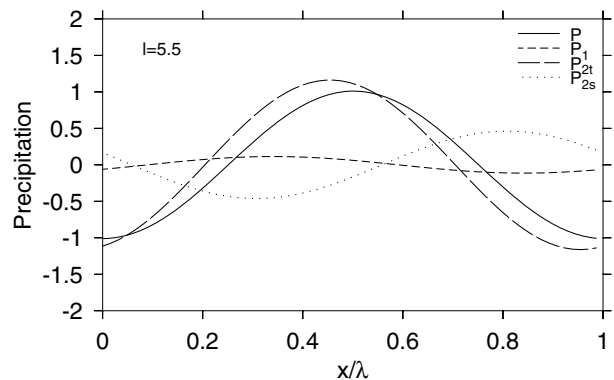


Fig. 12. Decomposition of precipitation as a function of wave phase for the eastward-moving convectively coupled gravity mode with zonal wavenumber $l = 5.5$ and with WISHE turned on.

largely set by the upper radiation boundary condition. Very little of the precipitation is associated with precipitable water perturbations, that is, P_1 , in agreement with the near-invisibility of the equatorial Kelvin wave in the satellite-observed precipitable water field.

Some disagreement exists between our results and the observations of the TEPPS Kelvin wave. In particular, though DCIN shows a decrease a few days before the wave due to a decrease in s_f as predicted by the model, the picture gets more complicated within 24 h of the wave passage; increases in both s_{bl} and s_f result in DCIN remaining near zero. Perhaps s_{bl} increases at least partially because of increased surface fluxes, and s_f follows as the resulting convection stabilizes the environment.

The moisture mode has very different characteristics. For large wavenumbers ($l = 10$) the precipitation is almost completely associated with P_1 , or precipitable water anomalies, as Fig. 13 shows. Changes in CIN due to changes in buoyancy of air above the PBL (P_{2t}) are negligible and only a small amount of precipitation comes directly from surface fluxes (P_{2s}). As with the gravity mode, this contribution is in quadrature with the primary heating, resulting in weak propagation to the east.

For longer wavelengths ($l = 2$), the picture is more complicated. Buoyancy anomalies above the PBL (P_{2t}) have a somewhat larger effect, but are still minor compared to the effect of precipitable water anomalies. However, surface fluxes play a much larger direct role, with P_{2s} being almost as large in magnitude

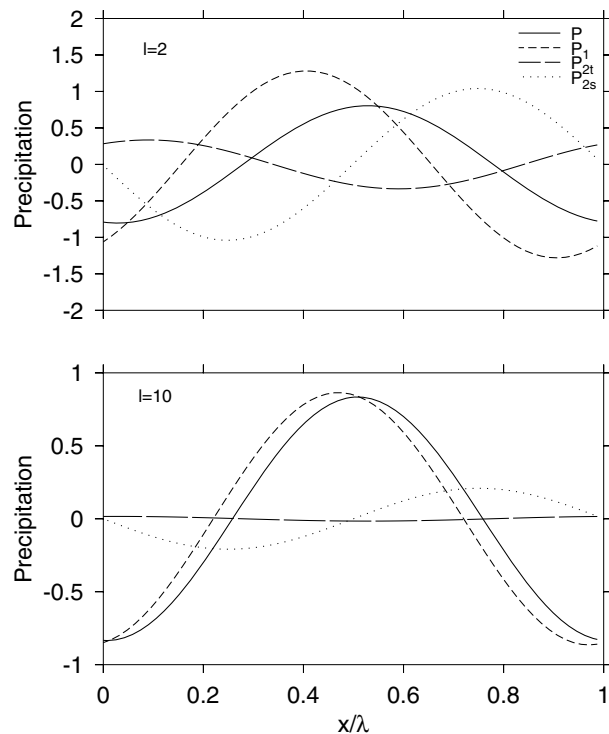


Fig. 13. As in Fig. 12 except for moisture mode with zonal wavenumbers $l = 2$ (upper panel) and $l = 10$ (lower panel).

as P_1 . This is again in quadrature with P_1 , so it acts primarily to induce the eastward propagation of moisture modes at long wavelengths.

6. Conclusions

This paper presents a minimal model for convectively coupled tropical disturbances in a non-rotating environment. The rainfall rate produced by the model is a function of both tropospheric precipitable water and convective inhibition, as suggested by observation. Two types of unstable modes are predicted by this model, a slowly moving ‘moisture mode’ in which the primary control of precipitation is the precipitable water, and a more rapidly propagating ‘gravity mode’ in which precipitation is controlled primarily by changes in convective inhibition associated with wave-induced buoyancy anomalies just above the planetary boundary layer. The gravity mode has almost the same zonal dynamics as equatorial Kelvin waves and inferences about the eastward-moving branch of the former can be applied to the latter mode. The gravity mode is relatively insensitive to WISHE.

Two elements distinguish the present model from its predecessors. First, the model is able to produce both the moisture mode and the convectively coupled gravity mode. Second, the model reproduces the observed structure of the gravity mode without imposing it a priori via complicated heating profiles associated with shallow convection and stratiform rain.

The first element arises from the observationally driven realization that both convective inhibition and tropospheric precipitable water act to control precipitation. Our results suggest that different types of atmospheric phenomena over tropical oceans act to produce precipitation primarily through one or the other of these mechanisms.

The second element constitutes a major simplification over the models of Mapes (2000), Majda and Shefter (2001b), Khouider and Majda (2006), etc., in which the two-mode vertical structure of the equatorial Kelvin wave is linked to a similar two-mode structure in the vertical heating profile. Our model shows that a simple first baroclinic mode heating profile is sufficient by itself to produce the observed two-mode structure of the Kelvin wave.

This gets to a fundamental point of convectively coupled Kelvin wave dynamics: Does the observed two-mode vertical structure result from the cloud physics of stratiform rain areas or does it come from the intrinsic dynamics of the Kelvin wave itself? Our results point to the latter and further suggest that the evolution of cloud behaviour through the life cycle of a Kelvin wave passage is governed primarily by wave dynamics rather than cloud physics. The mechanisms by which this occurs are still being sorted out, but the recent results of Tulich et al. (2007) may point the way.

The moisture mode produced by the current model is very similar to that seen in models which omit the dependence of precipitation rate on convective inhibition, such as Fuchs and Raymond (2002, 2007). Identification of this mode with actual

tropical disturbances is still in question, but Sobel et al. (2001) suggest many possible candidates. One difference between our results and those of Sobel et al. (2001) is that negative gross moist stability (or at least a negative equivalent gross moist stability including the effects of cloud-radiation interactions) is needed to destabilize the moisture mode in our case. However Sobel et al. (2001) show that moisture modes can become unstable in a three-dimensional, rotating environment exhibiting meridional moisture gradients even when the gross moist stability is positive. The difference between our model and that of Sobel et al. (2001) lies primarily in the large-scale dynamics and not in the precipitation closure.

The propagation speed of the gravity mode ($\approx 18\text{--}19\text{ m s}^{-1}$) is comparable to observed Kelvin wave propagation speeds, and for a reasonable choice of model parameters the maximum growth rate occurs near the zonal wavenumber of observed maximum spectral energy for this mode ($l \approx 5\text{--}7$). Furthermore, the tilted vertical structure of the temperature perturbation agrees with observations. These factors suggest that our model comes close to capturing the essential physics of convectively coupled equatorial Kelvin waves.

7. Acknowledgments

We thank the University of Washington Mesoscale Group for making TEPPS sounding data available on their web site. Comments by George Kiladis and another reviewer improved the paper significantly. This work was supported by U.S. National Science Foundation Grant ATM-0352639.

References

- Back, L. E. and Bretherton, C. S. 2005. The relationship between wind speed and precipitation in the Pacific ITCZ. *J. Climate* **18**, 4317–4328.
- Bony, S. and Emanuel, K. A. 2005. On the role of moist processes in tropical intraseasonal variability: cloud-radiation and moisture-convection feedbacks. *J. Atmos. Sci.* **62**, 2770–2789.
- Bretherton, C. S., Peters, M. E. and Back, L. E. 2004. Relationships between water vapor path and precipitation over the tropical oceans. *J. Climate* **17**, 1517–1528.
- Chang, C.-P. 1977. Viscous internal gravity waves and low-frequency oscillations in the tropics. *J. Atmos. Sci.* **34**, 901–910.
- Chang, C.-P. and Lim, H. 1988. Kelvin wave-CISK: a possible mechanism for the 30-50 day oscillations. *J. Atmos. Sci.* **45**, 1709–1720.
- Derbyshire, S. H., Beau, I., Bechtold, P., Grandpeix, J.-Y., Piriou, J.-M., and co-authors. 2004. Sensitivity of moist convection to environmental humidity. *Quart. J. Roy. Meteor. Soc.* **130**, 3055–3079.
- Emanuel, K. A. 1987. An air-sea interaction model of intraseasonal oscillations in the tropics. *J. Atmos. Sci.* **44**, 2324–2340.
- Emanuel, K. A. 1993. The effect of convective response time on WISHE modes. *J. Atmos. Sci.*, **50**, 1763–1775.
- Firestone, J. and Albrecht, B. A. 1986. The structure of the atmospheric boundary layer in the central equatorial Pacific during FGGE. *Mon. Wea. Rev.* **114**, 2219–2231.
- Fuchs, Ž. and Raymond, D. J. 2002. Large-scale modes of a nonrotating atmosphere with water vapor and cloud-radiation feedbacks. *J. Atmos. Sci.* **59**, 1669–1679.
- Fuchs, Ž. and Raymond, D. J. 2005. Large-scale modes in a rotating atmosphere with radiative-convective instability and WISHE. *J. Atmos. Sci.* **62**, 4084–4094.
- Fuchs, Ž. and Raymond, D. J. 2007. A simple, vertically resolved model of tropical disturbances with a humidity closure. *Tellus* **59A**, 344–354.
- Grabowski, W. W. 2003. MJO-like coherent structures: sensitivity simulations using the cloud-resolving convection parameterization (CRCP). *J. Atmos. Sci.* **60**, 847–864.
- Grabowski, W. W. and Moncrieff, M. W. 2004. Moisture-convection feedback in the tropics. *Quart. J. Roy. Meteor. Soc.* **130**, 3081–3104.
- Hayashi, Y. 1970. A theory of large-scale equatorial waves generated by condensation heat and accelerating the zonal wind. *J. Meteor. Soc. Japan* **48**, 140–160.
- Hayashi, Y. 1971a. Instability of large-scale equatorial waves under the radiation condition. *J. Meteor. Soc. Japan*. **49**, 315–318.
- Hayashi, Y. 1971b. Instability of large-scale waves with a frequency-dependent cisk parameter. *J. Meteor. Soc. Japan*. **49**, 59–62.
- Hayashi, Y. 1971c. Large-scale equatorial waves destabilized by convective heating in the presence of surface friction. *J. Meteor. Soc. Japan* **49**, 458–466.
- Khouider, B. and Majda, A. J. 2006. A simple multicloud parameterization for convectively coupled tropical waves. Part I: linear analysis. *J. Atmos. Sci.*, **63**, 1308–1323.
- Lindzen, R. S. 1967. Planetary waves on beta-planes. *Mon. Wea. Rev.* **95**, 441–451.
- Lindzen, R. S. 1974. Wave-CISK in the tropics. *J. Atmos. Sci.* **31**, 156–179.
- Lucas, C., Zipser, E. J. and Ferrier, B. S. 2000. Sensitivity of tropical west Pacific oceanic squall lines to tropospheric wind and moisture profiles. *J. Atmos. Sci.* **57**, 2351–2373.
- Madden, R. A. and Julian, P. R. 1994. Observations of the 40-50 day tropical oscillation—a review. *Mon. Wea. Rev.* **122**, 814–837.
- Majda, A. J., Khouider, B., Kiladis, G. N., Straub, K. H. and Shefter, M. G. 2004. A model for convectively coupled tropical waves: nonlinearity, rotation, and comparison with observations. *J. Atmos. Sci.* **61**, 2188–2205.
- Majda, A. J. and Shefter, M. G. 2001a. Waves and instabilities for model tropical convective parameterizations. *J. Atmos. Sci.* **58**, 896–914.
- Majda, A. J. and Shefter, M. G. 2001b. Models for stratiform instability and convectively coupled waves. *J. Atmos. Sci.* **58**, 1567–1584.
- Mapes, B. E. 1993. Gregarious tropical convection. *J. Atmos. Sci.*, **50**, 2026–2037.
- Mapes, B. E. 2000. Convective inhibition, subgrid-scale triggering energy, and stratiform instability in a toy tropical wave model. *J. Atmos. Sci.* **57**, 1515–1535.
- Mapes, B. E. and Houze, R. A. Jr. 1995. Diabatic divergence profiles in western Pacific mesoscale convective systems. *J. Atmos. Sci.*, **52**, 1807–1828.
- Matsuno, T. 1966. Quasi-geostrophic motions in the equatorial area. *J. Meteor. Soc. Japan* **44**, 25–43.
- McBride, J. L. and Frank, W. M. 1999. Relationships between stability and monsoon convection. *J. Atmos. Sci.* **56**, 24–36.

- Miller, M. J., Beljaars, A. C. M. and Palmer, T. N. 1992. The sensitivity of the ECMWF model to the parameterization of evaporation from the tropical oceans. *J. Climate* **5**, 418–434.
- Neelin, J. D. and Held, I. M. 1987. Modeling tropical convergence based on the moist static energy budget. *Mon. Wea. Rev.* **115**, 3–12.
- Neelin, J. D. and Yu, J.-Y. 1994. Modes of tropical variability under convective adjustment and the Madden-Julian oscillation. Part I: analytical theory. *J. Atmos. Sci.* **51**, 1876–1894.
- Peters, M. E. and Bretherton, C. S. 2006. Structure of tropical variability from a vertical mode perspective. *Theor. Comput. Fluid Dyn.*, **20**, 501–524, DOI 10.1007/s00162-006-0034-x.
- Ramage, C. S. 1971. *Monsoon Meteorology*. Academic Press, New York, pp. 296.
- Raymond, D. J. 1995. Regulation of moist convection over the west Pacific warm pool. *J. Atmos. Sci.* **52**, 3945–3959.
- Raymond, D. J., Raga, G. B., Bretherton, C. S., Molinari, J., López-Carrillo, C. and co-authors. 2003. Convective forcing in the intertropical convergence zone of the eastern Pacific. *J. Atmos. Sci.* **60**, 2064–2082.
- Raymond, D. J., Esbensen, S. K., Paulson, C., Gregg, M., Bretherton, C. S. and co-authors. 2004. EPIC2001 And the coupled ocean-atmosphere system of the tropical east Pacific. *Bull. Am. Meteor. Soc.* **85**, 1341–1354.
- Raymond, D. J. and Zeng, X. 2005. Modelling tropical atmospheric convection in the context of the weak temperature gradient approximation. *Quart. J. Roy. Meteor. Soc.* **131**, 1301–1320.
- Roundy, P. E. and Frank, W. M. 2004. A climatology of waves in the equatorial region. *J. Atmos. Sci.* **61**, 2105–2132.
- Sobel, A. H., Yuter, S. E., Bretherton, C. S. and Kiladis, G. N. 2004. Large-scale meteorology and deep convection during TRMM KWAJEX. *Mon. Wea. Rev.* **132**, 422–444.
- Sobel, A. H. and Horinouchi, T. 2000. On the dynamics of easterly waves, monsoon depressions, and tropical depression type disturbances. *J. Meteor. Soc. Japan* **78**, 167–173.
- Sobel, A. H., Nilsson, J. and Polvani, L. M. 2001. The weak temperature gradient approximation and balanced tropical moisture waves. *J. Atmos. Sci.* **58**, 3650–3665.
- Straub, K. H. and Kiladis, G. N. 2002. Observations of a convectively coupled Kelvin wave in the eastern Pacific ITCZ. *J. Atmos. Sci.* **59**, 30–53.
- Tulich, S. N., Randall, D. A. and Mapes, B. E. 2007. Vertical-mode and cloud decomposition of large-scale convectively coupled gravity waves in a two-dimensional cloud-resolving model. *J. Atmos. Sci.*, **64**, 1210–1229.
- Wang, B. and Rui, H. 1990. Dynamics of the coupled moist Kelvin-Rossby wave on an equatorial beta plane. *J. Atmos. Sci.* **47**, 397–413.
- Wheeler, M., Kiladis, G. N. and Webster, P. J. 2000. Large-scale dynamical fields associated with convectively coupled equatorial waves. *J. Atmos. Sci.* **57**, 613–640.
- Wheeler, M. and Kiladis, G. N. 1999. Convectively coupled equatorial waves: analysis of clouds and temperature in the wavenumber-frequency domain. *J. Atmos. Sci.* **56**, 374–399.
- Yano, J.-I. and Emanuel, K. A. 1991. An improved model of the equatorial troposphere and its coupling with the stratosphere. *J. Atmos. Sci.* **48**, 377–389.
- Yuter, S. E. and Houze, R. A. Jr. 2000. The 1997 Pan American Climate Studies tropical eastern Pacific process study. Part I: ITCZ region. *Bull. Am. Meteor. Soc.* **81**, 451–481.